Nano Energy 119 (2024) 109049

Contents lists available at ScienceDirect

Nano Energy

journal homepage: www.elsevier.com/locate/nanoen

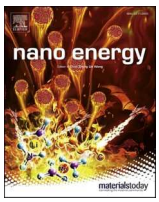

Full paper

Pathway to high performance, low temperature thin-film solid oxide cells grown on porous anodised aluminium oxide

Matthew P. Wells [a,*], Adam J. Lovett [a], Yizhi Zhang [b], Zhongxia Shang [b], Kosova Kreka [c], Babak Bakhit [a,d,e], Haiyan Wang [b], Albert Tarancón [c,f], Judith L. MacManus-Driscoll [a]

[a] Department of Materials Science and Metallurgy, University of Cambridge, 27 Charles Babbage Road, Cambridge CB3 0FS, United Kingdom
[b] School of Materials Engineering, Purdue University, 701 West Stadium Avenue, West Lafayette, IN 47907-2045, United States
[c] Catalonia Institute for Energy Research (IREC), Department of Advanced Materials for Energy, 1 Jardins de les Dones de Negre, Barcelona 08930, Spain
[d] Thin Film Physics Division, Department of Physics (IFM), Linköping University, Linköping SE-58183, Sweden
[e] Electrical Engineering Division, Department of Engineering, University of Cambridge, JJ Thomson Avenue, Cambridge CB3 0FA, United Kingdom
[f] ICREA, Passeig Lluís Companys 23, Barcelona 08010, Spain

ARTICLE INFO

Keywords:
Vertically aligned nanocomposite film
Solid oxide cell
Oxygen vacancy
High-performance
Pulsed laser deposition

ABSTRACT

Reversible solid oxide cells (rSOCs) present a promising solution to future energy challenges through the efficient conversion between electrical and chemical energy. To date, the benefits of rSOC technology have been off-limits to portable power and electrolysis applications due to the excessive polarisation resistance of the oxygen electrode at low temperatures, characterised by high area specific resistance (ASR) values below 500 °C. In this work we demonstrate growth of symmetric and complete rSOC structures based on state-of-the-art vertically aligned nanocomposite (VAN) films grown by pulsed laser deposition (PLD) on porous Pt-coated anodised aluminium oxide (AAO) substrates. The symmetric rSOC structures give the first demonstration of an rSOC oxygen electrode with ASR below 0.1 Ωcm^2 at temperatures less than 450 °C. This is achieved through oxygen vacancy tuning by annealing, as confirmed by Time-of-Flight Elastic Recoil Detection Analysis (ToF-ERDA) and Rutherford Backscattering Spectrometry (RBS) measurements. Thus, the present work describes a promising route towards future high-performance rSOC devices for portable power applications.

1. Introduction

Reversible solid oxide cells (rSOCs) offer a means of converting chemical to electrical energy, and vice versa, with high theoretical efficiency [1–3]. Therefore, rSOCs are widely considered to be a promising solution to the challenges faced in future portable power applications. However, despite extensive research efforts, the widespread implementation of rSOCs has been hindered by excessive polarisation resistances of the oxygen electrode, characterised by high area specific resistance (ASR) values, at the low temperatures (<500 °C) demanded by portable applications [3].

In order to reduce the ASR and improve the high temperature stability of rSOCs vertically aligned nanocomposite (VAN) films have emerged as a leading class of materials [4–9]. Not only can the desired high ionic and electronic conduction be individually achieved by using separate phases, but much improved performance characteristics can be achieved compared to planar thin films. This has been recently demonstrated in $La_{0.8}Sr_{0.2}MnO_3$-$Ce_{0.8}Sm_{0.2}O_2$ (LSM-SDC) VAN films, in which the SDC phase acts as a supply of oxygen vacancies to the LSM phase, resulting in a ~100 fold enhancement in oxygen incorporation kinetics and a drastically reduced ASR compared to planar LSM films [3].

To enable the formation of idealized VAN nanostructures, the majority of VAN systems studied to date have been deposited on single crystal substrates [4,6,9–13]. Recent years have, however, seen attempts to realise the advantages of VAN films on more commercially viable substrates such as stainless steel and porous anodised aluminium oxide (AAO) [8,14]. AAO substrates are advantageous, particularly at the proof-of-concept cell scale, as they can be manufactured at low cost with finely tuned, uniform pore sizes ranging from tens to hundreds of nanometres. They also mitigate the need for complex patterning steps in device fabrication. In particular, Lee et al. demonstrate the fabrication of a thin film rSOC with an $La_{0.6}Sr_{0.4}Co_{0.2}Fe_{0.8}O_3$-$(Y_2O_3)_{0.08}(ZrO_2)_{0.92}$ (LSCF-YSZ) VAN cathode deposited by co-sputtering of LSCF and YSZ on

* Corresponding author.
E-mail address: mpw52@cam.ac.uk (M.P. Wells).

https://doi.org/10.1016/j.nanoen.2023.109049
Received 22 December 2022; Received in revised form 13 October 2023; Accepted 28 October 2023
Available online 31 October 2023

AAO. The resulting device delivered a peak power density of 2.5 W.cm^{-2} at 650 °C, which the authors claim to be the highest recorded for a YSZ-based rSOC at this temperature[14]. Despite this progress however, such power densities remain off-limits to the low temperature operating regime required for a range of portable applications. Here, the sluggish kinetics of the oxygen reduction reaction typically dominate the overall cell impedance leading to high ASR values and thus reduced peak power densities. Typically, an ASR of 0.1 Ω cm^2 is considered desirable [15].

The aim of this work is to a develop a route to achieving minimised ASR in rSOCs for operation below 500 °C. To achieve this, symmetric rSOC structures based on state-of-the-art LSCF-SDC VAN oxygen electrodes were deposited as dense films by pulsed laser deposition (PLD) on porous thin film Pt-coated AAO substrates (Fig. 1(a)). We note here that there are two common challenges associated with Pt, namely cost and agglomeration at high temperatures (> 600 °C) [14,16]. In the case of a thin-film device, however, the cost is not necessarily prohibitive: for a 1.33 cm^2 device coated with 200 nm Pt as studied here, the cost of the Pt itself would be ~ $0.02 (based on a Pt cost of $30/g)). Meanwhile, the challenge of agglomeration could be mitigated by facilitating device operation below 500 °C. Herein, we also explore the impact of the oxide deposition at 600 °C and 700 °C on the Pt microstructure.

The design based on AAO substrates enables rSOC structures to be deposited with a thin electrolyte layer (~50 nm) and therefore facilitates probing of the oxygen electrode behaviour at low temperatures, without significant contribution from the electrolyte impedance. This unique device configuration facilitates the development of an annealing strategy to drastically reduce the ASR. As we show later, the annealing of the VAN electrodes in vacuum significantly increases the oxygen vacancy concentration in the films. This leads to the first demonstration of an ASR value <0.1 Ωcm^2 at temperatures below 450 °C. To the best of our knowledge, this marks the lowest recorded ASR for a low-temperature rSOC structure to date. We proceed to demonstrate that the same conditions used for annealing are suitable for the deposition of a YSZ-Ni nanocomposite fuel electrode (YSZ-Ni composites are widely used as fuel electrodes and offer state-of-the-art performance [17–20]). However, as we show later, further engineering studies are necessary to ensure mechanical stability of the thin-film device structures based on porous alumina. Nevertheless, by showing the way to the development of future rSOC devices with ASR values <0.1 Ω cm^2 below 500 °C, the present work provides a promising route towards future high-performance rSOC devices for portable power applications.

2. Experimental methods

Ceramic targets for pulsed laser deposition were prepared by grinding ~3 g powder using an agate pestle and mortar for 30 min. The powders were then pelletised using a 10 ton isostatic press and sintered at 1300 °C for 4 h, with a heating/cooling rate of 5 °C/min. YSZ targets were prepared using 3 g $(Y_2O_3)_{0.08}(ZrO_2)_{0.92}$ powder. LSCF-SDC, YSZ-STO, and YSZ-Ni targets were made by mixing 50:50 wt % $(La_{0.60}Sr_{0.40})_{0.95}Co_{0.20}Fe_{0.80}O_3$ and $(Sm_2O_3)_{0.20}(CeO_2)_{0.80}$, $(Y_2O_3)_{0.08}(ZrO_2)_{0.92}$ and $SrTiO_3$, and $(Y_2O_3)_{0.08}(ZrO_2)_{0.92}$ and NiO powders respectively. $(La_{0.60}Sr_{0.40})_{0.95}Co_{0.20}Fe_{0.80}O_3$ powder was supplied by Fuel cell materials, Nexceris, LLC, with all others supplied by Alfa Aesar.

Thin films were grown by pulsed laser deposition (PLD) on (001) oriented $(Y_2O_3)_{0.08}(ZrO_2)_{0.92}$ (CrysTec GmbH) and porous anodised aluminium oxide (Whatman) substrates. Before use, AAO substrates were coated with Pt by room temperature DC magnetron sputtering. Before each PLD process the chamber was evacuated to at least 7×10^{-7} mbar. Ceramic targets were held 45 mm from the substrates and ablated with a 248 nm KrF laser (Lambda Physik, Inc). LSCF-SDC and YSZ films were deposited at 600 °C with a repetition rate of 3 Hz in an atmosphere of 0.4 mBar O_2 with a gas flow rate of 6 sccm. For LSCF-SDC the laser fluence was ~3.2 J/cm^2 and for YSZ the fluence was ~1.6 J/cm^2. YSZ-Ni films were deposited under vacuum conditions (7×10^{-7} mBar) at 700 °C with a repetition rate of 3 Hz and influence of 0.3 J/cm^2. Samples were cooled to room temperature at 10 °C/min in the same

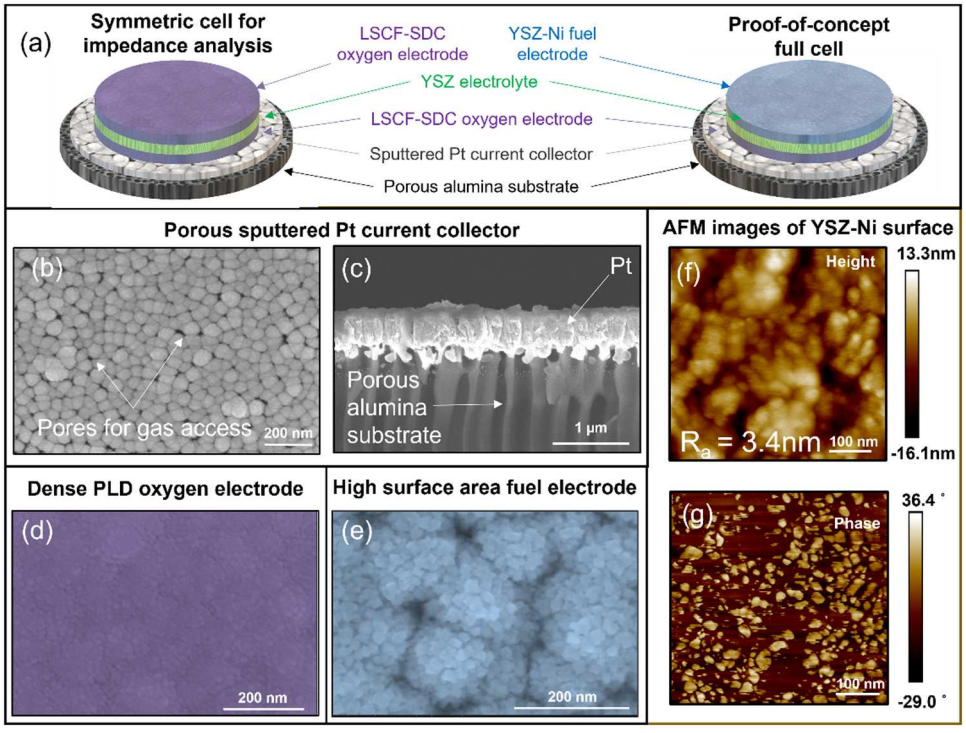

Fig. 1. a) Schematic of reversible solid oxide cell (rSOCs) structures developed in this work in both symmetric configuration [left] and proof-of-concept full cell configuration [right]; b) top-down SEM of porous Pt current collecting layer; c) cross-sectional SEM showing porous alumina substrate with porous Pt layer grown on top; d) top-down SEM of dense LSCF-SDC oxygen electrode layer; e) top-down SEM of dense YSZ-Ni fuel electrode layer; f) AFM height images of top YSZ-Ni fuel electrode layer; g) AFM phase image of top YSZ-Ni fuel electrode layer.

atmosphere in which they were grown. For multilayer samples, LSCF-SDC and YSZ layers were deposited sequentially without breaking vacuum or adjusting the substrate temperature. Prior to deposition of the YSZ-Ni layer samples were first cooled to 200 °C and the chamber filled with 800 mBar N_2 before evacuating again to 7×10^{-7} mBar and heating to the deposition temperature of 700 °C. These same conditions were also used for the annealing of LSCF-SDC films.

X-ray diffraction measurements were performed using a Panalytical Empyrean high resolution X-ray diffractometer using Cu-Kα radiation (λ = 1.5405 Å). A Bruker Multimode 8 system was used in tapping mode for AFM. Commercial silicon cantilevers (Budget Sensors Ltd) with a resonance frequency of 300 kHz and spring constant of 40 N/m were used to image 0.5 μm^2 areas at a scan frequency of 1 Hz.

Impedance spectroscopy measurements were conducted on symmetric cells using a Materials Lab XM Impedance Analyser (Ametek). Nyquist plots were acquired in air using a porous Au paste or sputtered Pt current collectors over a frequency range 10^6 – 1 Hz with a voltage amplitude of 10 mV. The acquired Nyquist plots were fitted to a modified Jamnik-Maier circuit comprising two ZARC elements (a resistor in parallel with a constant phase element) connected in series, as in comparable literature works [14].

Electron microscopy images were acquired using a Nova NanoSEM 450 system. Transmission Electron Microscopy (TEM), Scanning Transmission Electron Microscopy (STEM) and STEM electron-dispersive X-ray spectroscopy (EDX) were performed with a FEI TALOS 200X operated at 200 kV, and FEI Titan™ G2 80–200 STEM with a Cs probe corrector and ChemiSTEM™ technology, operated at 200 kV. STEM images were taken with a high-angle annular dark-field (HAADF) detector with a collection range of 60–160 mrad.

Measurements of complete SOC structures were attempted using a ProboStat™ (NorECS) system with dry H_2 and O_2 supplied to the fuel and oxygen electrodes respectively at rates of 120 and 50 Nml min^{-1} cm^{-2}. A gas-tight seal between the fuel and oxygen electrodes was attempted by application of Ceramabond™ paste (Aremco) around the AAO-based device structure.

Time-of-flight elastic recoil detection analyses (ToF-ERDA) and Rutherford backscattering spectrometry (RBS) were carried out in a 5-MV 15SDH-2 tandem accelerator on as-deposited and vacuum-annealed LSCF-SDC thin films grown on Si(001) substrates. In the ToF-ERDA measurements, recoils were detected at an angle of 45° with respect to the incident beam in a telescope that measured ToF (using a foil-detector) and energy (in a gas ionization chamber in coincidence). This approach provides mass resolved data in the plots of ToF vs Energy. Recoils were created using a 36-MeV $^{127}I^{8+}$ beam incident at 67.5° with respect to the sample surface normal. Elemental depth-profiles and average elemental compositions are determined from ToF-ERDA time-energy coincidence spectra using CONTES and Potku software packages. 2-MeV $^4He^+$ ions were employed for the RBS measurements, in which backscattered ions were detected at a scattering angle of 170°. The possible ion-channelling effects in both substrates and thin films were minimised by adjusting the incidence angle to 5° with respect to the surface normal and performing multiple-small-random-angular movements within a range of 2° during data acquisition [21]. SIMNRA, version 7.02, was used for simulating the RBS spectra and obtaining the elemental compositions of the films. The maximum systematic uncertainty in both techniques from the effect of stopping cross-sections is < 0.7 %, while the maximum statistic uncertainties arising from the number of experimental counts are < 0.9 %.

3. Results and discussion

For testing electrochemical performance, LSCF-SDC VAN films were grown in a symmetric configuration, consistent with previous studies of high performing SOFC cathode materials.[3,22,23] The films were supported by a porous anodised aluminium oxide (AAO) substrate, on top of which a porous Pt current collecting layer was deposited by room temperature magnetron sputtering. Each layer was deposited by PLD in a single step process without breaking vacuum. Samples were deposited in this manner both with, and without, an annealing step performed at 700 °C at 7×10^{-7} mbar. Finally, a proof-of-concept rSOC structure was grown in the same manner comprising LSCF-SDC, YSZ, and YSZ-Ni as the oxygen electrode, electrolyte, and fuel electrode respectively. In this case, the deposition process was designed to simultaneously provide optimal deposition conditions for the YSZ-Ni and for the effective annealing of the already deposited oxygen electrode layer. Thus, the oxygen electrode could be annealed in-situ at the time of deposition.

The growth mechanism of Pt sputtered onto porous AAO substrates is explored in detail by Shaban et al., where Pt is shown to nucleate in a connected, nanoporous hexagonal array around the AAO pore [24]. Here, the porosity of the sputtered Pt current collecting layer is shown from the cross-sectional and top-down SEM images in Fig. 1(b) and (c) respectively, with pores approximately 5–20 nm observed between Pt grains. We note that the porous structure here is reminiscent of recently developed 'nanoporous' Pt SOFC cathodes, featuring pore dimensions in the < 10 nm regime with porosity ~25 % [25–27]. Using SEM image analysis software, we estimate the porosity to be ~9 %.

Fig. 1(d) demonstrates that a dense and defect free surface of the oxygen electrode layer is achieved. The dense structure can intuitively be attributed to the fact that PLD is not a conformal process, and hence lateral growth over the pores is expected. Also, since the grain size of the PLD film is greater than the size of the pores between the Pt grains in Fig. 1(b), the lateral growth of the grains is complete across the pores. Here we note the importance of careful design of the substrate pore size; Fig. S1 reveals the effect of Pt deposition on AAO substrates with pore diameters of 20 and 200 nm, with the subsequent growth of a dense film by PLD *only* possible in the former case.

Finally, Fig. 1(e) and (f) show SEM and AFM images, respectively, demonstrating the high surface area structure achieved following deposition of the YSZ-Ni fuel electrode, while the AFM phase response (Fig. 1(g)) shows 2 different regions of contrast with the lighter shaded regions of ~15–30 nm diameter consistent with the formation of a nanocomposite structure.

The thin film rSOC structures were further characterised by TEM, as shown in Fig. 2. High angle annular dark field (HAADF)-STEM imaging (Fig. 2(a)) reveals that the LSCF-SDC film adopts a vertically aligned nanocomposite structure, despite the growth on polycrystalline AAO substrates (as opposed to the single-crystal substrates of many previous works [3,4,6,7,10,11]). Meanwhile, EDX mapping images (Fig. 2(b)-(e)) confirm the deposition of a thin (< 50 nm), dense Zr-based electrolyte layer atop the 200 nm LSCF-SDC. Finally, Fig. 2(f) shows a higher magnification image revealing the separation between the electrolyte and YSZ-Ni fuel electrode layers, as indicated by the white dashed lines. Here, the interface between the background and the YSZ-Ni film surface is determined from the STEM image.

The rSOC structures are further studied by XRD in Fig. S2, where Fig. S2(a) and (b) show results collected from 2θ-ω and grazing incidence scans, respectively. Here we observe the polycrystalline nature of the rSOC structures on AAO, which is as expected for growth on non-single crystal substrates. Fig. S2 shows scans of samples before and after annealing, from which we observe no significant structural changes. The XRD results of films grown on single-crystal YSZ substrates are also shown (Fig. S3) from which we confirm the epitaxial growth of the LSCF and SDC phases in the expected (hk0) and (h00) directions respectively.

The performance of the LSCF-SDC oxygen electrodes is characterised by electrochemical impedance spectroscopy (EIS). To be certain of correct interpretation of the impedance data, a number of comparator samples were grown on both single-crystal YSZ and porous AAO substrates. For ease of reference, these comparator samples are labelled A-F as detailed in Table 1 below; all samples deposited on single-crystal YSZ substrates are denoted by square symbols, while circles denote samples grown on porous AAO. The ASRs of each sample were calculated from

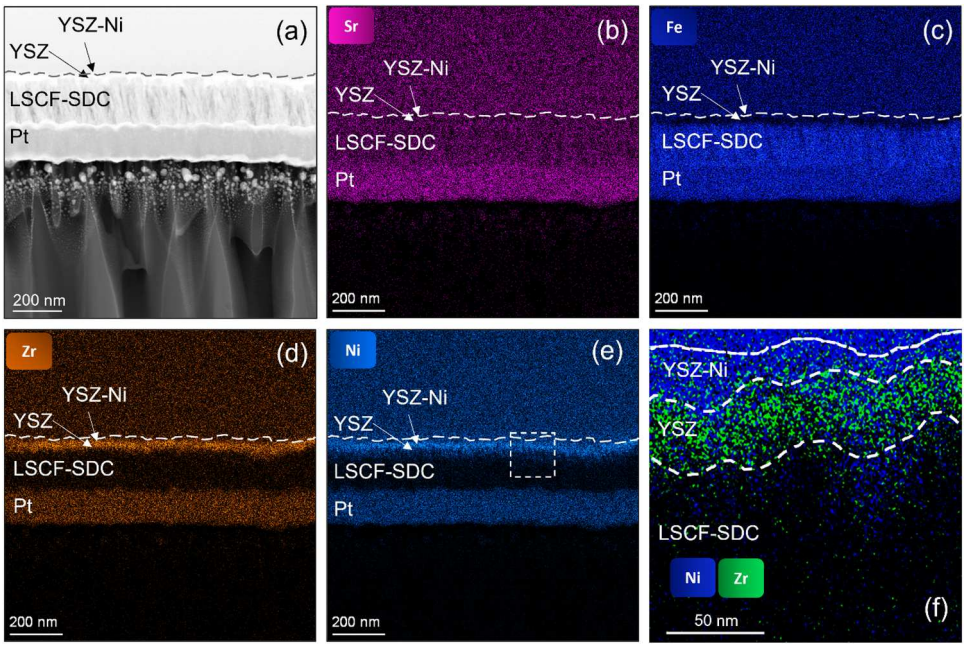

Fig. 2. a) HAADF-STEM image showing vertically aligned nanostructure of LSCF-SDC oxygen electrode layer; b – e) EDX mapping images confirming desired oxygen electrode, electrolyte, fuel electrode structure; f) higher magnification image showing distinction between electrolyte and fuel electrode layers.

the impedance data and Fig. 3(a) shows the comparison of samples B, D, and E, with respect to previous literature; Fig. 3(b) shows the Nyquist plots for sample E over a range of measurement temperatures; Fig. 3(c) and (d) respectively show Arrhenius and Nyquist plots describing the evolution of the ASR as a function of time spent at 430 °C.

3.1. Sample A and B: comparison to literature of LCSF-SDC VAN films with Au and Pt current collectors

Several previous works have highlighted the substantial impact of the current collector on the measured impedance [28]. In particular, Boukamp et al. demonstrate that a reduction in ASR of at least an order of magnitude may be observed in LSCF when using a Pt rather than Au current collector [32]. We therefore begin by comparing samples A and B, the difference being only the current collector, i.e. Au (A) versus Pt (B). From Fig. S4, there is only a slight reduction in ASR for the Pt current collector compared to Au, thus indicating that the dominant impedance response is that of the LSCF-SDC, with little influence of the noble metal.

We next consider samples A and B with reference to previous literature [8,28,30,31]. Here, the gold paste current collecting layer of A provides an equivalent experimental set up to previous studies of thin film SOFC cathode materials [3,8], while the Pt current collector of B provides a valid comparison to the studies of bulk LSCF by Shen et al. [31]. The existing literature regarding LSCF and LSCF-based composites presents a wide variety of ASR and activation energy (E_a) values, particularly between bulk and thin-film samples. For bulk LSCF reported E_a values range from 0.4 eV [31] to 1.5 eV [22] compared to between 1.6 eV and 2.4 eV for thin films [28], with differences attributed to the high Sr surface content in thin films, resulting from segregation during high temperature growth [33,34]. Recent works however have shown that the E_a of LSCF thin films can be successfully reduced to 0.4 eV using a post-deposition surface treatment to remove excess Sr content at the film surface [34]. Meanwhile, VAN structures (LSM-SDC) have been shown to inhibit the formation of excess surface Sr during growth [3]. In this context, it is unsurprising that our LSCF-SDC VAN samples A and B exhibit $E_a \approx 1.1$ eV, as observed in Fig. 3(a). This is an exceptionally low value for thin-film samples and highlights the suitability of the LSCF-SDC nanocomposite for low-temperature operations.

In terms of ASR, from Fig. 3(a) we observe values of ~60 Ωcm^2 at 500 °C, competitive with state-of-the-art porous, surface treated LSCF thin films, also grown on YSZ single crystals [8]. Further, as expected, the high temperature ASR for the thin-film LSCF-SDC is higher than for the equivalent bulk nanocomposite of the same composition prepared by screen-printing [32] (~3x higher at 500 °C). The low activation energy of ~1.1 eV however results in comparable ASR values at lower temperatures.

3.2. Sample C: comparison of cathodic response of LSCF-SDC VAN to Pt

To be further sure that the Pt layer is not the dominating active layer, an additional cell was fabricated on AAO with just Pt as the oxygen electrode (D), i.e. without the LSCF-SDC VAN layer. As shown in Fig. S4, the ASR values for this cell agree with literature reports for Pt films of comparable thickness grown on YSZ. Fig. S4 also shows that the ASR of cell C is significantly higher than for A, B, D and E, which all incorporate an LSCF-SDC layer, thereby confirming the critical role of the LSCF-SDC VAN film in enhancing the rate of the cathodic reduction above that achieved by Pt, Pt being rate-limited by grain boundary oxygen diffusion [35,36].

3.3. Sample D: comparison of cells grown on AAO and YSZ single crystal substrates

The ASR values of LSCF-SDC films grown on AAO (D) and single-crystal YSZ substrates (B) are now compared in Fig. 3(a). As already discussed and shown in Fig. S2, growth of the VAN layer on single crystal YSZ gives epitaxial growth of both LSCF and SDC phases with (hk0) and (h00) out-of-plane orientations, respectively, whereas the VAN film on AAO shows only oriented (i.e. (111) and (200) LSCF and (321) YSZ), textured out-of-plane growth (Fig. S3). Nonetheless, both samples exhibit comparable ASR values; this is consistent with previous works which have demonstrated approximately a 2.5 factor enhancement in the chemical exchange coefficient of (111) compared to (110) oriented LSCF. This may be sufficient to counteract any deleterious effects associated with lower crystallinity films [37]. In terms of YSZ, it has been shown previously that different crystallographic orientations can substantially affect the ionic conductivity, however in this case, as the

Table 1
Summary of samples for EIS analysis.

Sample reference	Substrate	Cell structure	Schematic	Symbol in Fig. 3 (a) / Fig. S5
A	Single-crystal YSZ	Au/LSCF-SDC/YSZ/LSCF-SDC/Au	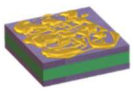	■
B	Single-crystal YSZ	Pt/LSCF-SDC/YSZ/LSCF-SDC/Pt	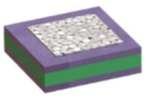	◆
C	Porous AAO	Pt/YSZ/Pt	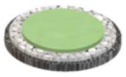	○
D	Porous AAO	Pt/LSCF-SDC/YSZ/LSCF-SDC/Pt	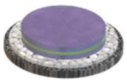	●
E	Porous AAO	Pt/LSCF-SDC/YSZ/LSCF-SDC/Pt - annealed		●
F	Porous AAO	Pt/LSCF-SDC/YSZ/YSZ-Ni	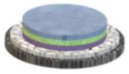	●

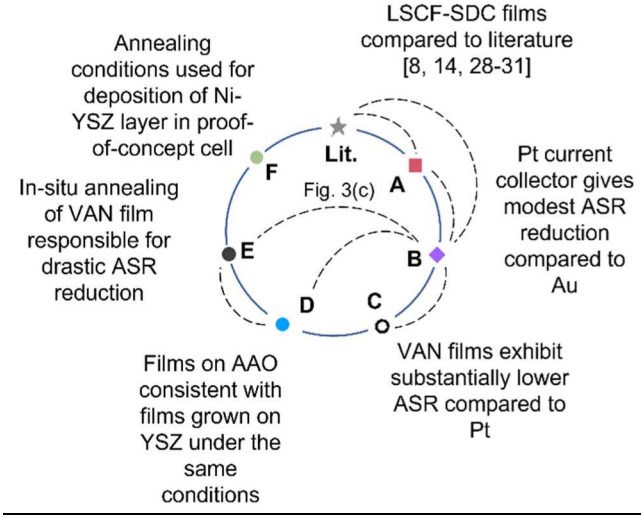

impedance is dominated by the electrode response, this effect is considered to be negligible[38]. It is also notable that a comparison between samples A and D suggest a minimal impact of the low porosity (~9 %) of the sputtered Pt current collecting layer compared to the more typical Au-paste used in sample A. We also note here the comparison to the recent work of Lee et al., whose cell structure provides a close comparison to sample D. Specifically, Lee et al. present a LSCF-YSZ/GDC/YSZ/Ni-YSZ structure grown by co-sputtering on AAO substrates which delivers a peak power density of 2.5 W.cm^{-2} at 650 °C, the highest recorded for a YSZ-based rSOC at this temperature. By assuming a linear extrapolation of the ASR values reported by Lee et al. we can see that the values achieved for sample D are close in comparison. [35,36].

3.4. Sample E: comparison of cells before and after annealing

We next consider the annealed LSCF-SDC films; by comparing the ASR of sample E to literature values for conventional dense LSCF thin films [28], state-of-the-art porous LSCF thin films [8], and a bulk LSCF-SDC nanocomposite [30] a remarkable reduction in ASR is revealed in Fig. 3(a). An ASR of 0.1 Ωcm^2 is achieved at ~425 °C, where there is a reduction in ASR of 2–3 orders of magnitude *c.f.* previous state-of-the-art materials. To the best of our knowledge, this marks the first demonstration of an ASR value < 0.1 Ωcm^2 at temperatures below 500 °C.

The drastic reduction in ASR of the annealed compared to the non-annealed LSCF-SDC films is further highlighted by comparing the Nyquist plots of samples B and E in Fig. S5. Here, sample B is measured at 420 °C while sample E is measured at 210 °C. The Nyquist plots for both films are dominated by the LSCF-SDC surface response, indicated by a capacitance of the low frequency arc on the order of 1×10^{-6} - 1×10^{-4} F.cm^{-2} in both cases [39]. Despite the fact the annealed LSCF-SDC is operating at a 210 °C lower temperature than the non-annealed LSCF-SDC, it is observed that the semicircle features corresponding to the LSCF-SDC cathodic response are almost identical, thus highlighting the significantly enhanced cathodic reaction rate achieved by the annealing process.

We note that samples grown on single crystal YSZ and on AAO can both be fitted by the same equivalent circuit typical of comparable VAN-based devices [3,14,40] (two resistors and constant phase elements in parallel as shown in Fig. 3(b) (an additional series resistor is included for the fitting of samples grown on AAO to account for the impedance of the experimental setup. However, this contribution is negligible for samples grown on single crystal YSZ)). The fitted parameters are provided in Table S1 and S2. Samples on YSZ reveal features of two distinct characteristic capacitances, on the order of 1×10^{-10} F.cm^{-2} and 1×10^{-4} F.cm^{-2}. The former is ascribed to the bulk ionic conductivity of the YSZ substrate and the latter to the oxygen reduction reaction and charge transfer process at the electrode/electrolyte interface for both LSCF-SDC electrodes of the symmetric structure.[22,23] We note here the conductivity of the YSZ substrate, calculated from the high frequency arc, is consistent with literature values for YSZ [41]. For samples on AAO both characteristic capacitances are consistent with assignment to the oxygen reduction reaction and charge transfer processes. Owing to the thin film electrolyte, the contribution of the bulk ionic transport is small, and cannot be reliably determined. The ASR of the LSCF-SDC films grown on YSZ and AAO are therefore calculated by Eqs. 1 and 2 respectively:

$$ASR = Area \times \left(\frac{R_2}{2}\right) \quad (1)$$

$$ASR = Area \times \left(\frac{R_1 + R_2}{2}\right) \quad (2)$$

In addition to the literature comparisons provided in Fig. 3, Table 2 below summarises the ASR and activation energy values of a range of cathode/oxygen electrode materials presented in literature to date.

3.5. Understanding the enhanced rSOC performance (sample E)

To understand the exceptional low temperature ASR performance of the annealed LSCF-SDC, we consider the influence of the annealing step. Oxygen vacancies are well known to form in LSCF at 700 °C under reduced oxygen partial pressures. Mantzavinos et al. show that, for pO_2 ~7×10^{-3} Torr at 700 °C, $\delta = 0.075$ in bulk $La_{0.6}Sr_{0.4}Co_{0.2}Fe_{0.8}O_{3-\delta}$ [44]. One would therefore expect a substantial change in oxygen stoichiometry for thin film LSCF under the lower oxygen partial pressures used here.

In recent years, the availability of oxygen vacancies has been shown to be critical to the oxygen reduction kinetics of cathodic thin films [3,45,46]. In particular, Cao et al. reveal, through ab-initio calculations, surface O_2 dissociation up to 3 orders of magnitude faster in $La_{0.5}Sr_{0.5}CoO_{3-\delta}$ with CoO_2 termination, compared to (La,Sr)O termination, due to the high oxygen vacancy concentration of the former [46]. This is widely supported by several experimental works

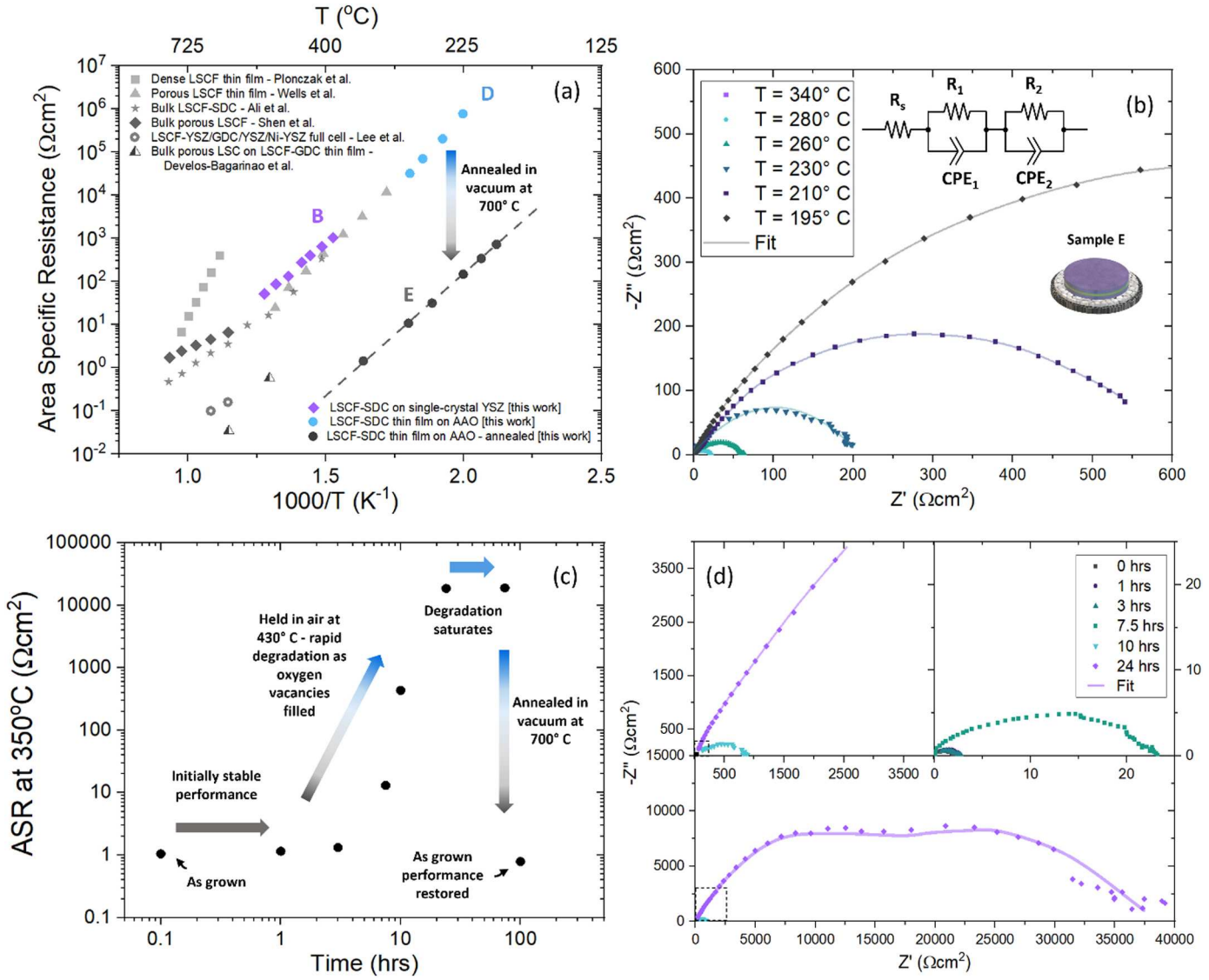

Fig. 3. a) Arrhenius plots comparing LSCF-SDC thin films deposited on single crystal YSZ and Pt-coated porous AAO substrates before and after annealing [8,14,28–31]; b) representative Nyquists plot of LSCF-SDC / YSZ / LSCF-SDC cell; c) stability measurements of LSCF-SDC / YSZ / LSCF-SDC cell showing evolution of ASR values with time spent at 430 °C; d) Nyquist plots showing evolution of impedance spectra as a function of time spent at 430 °C.

Table 2
Comparison of ASR and activation energies of high-performance oxygen electrode materials from literature. An asterisk denotes that data have been extrapolated to provide comparison at 500 °C.

Material	Thickness	ASR at 500 °C (Ωcm^2)	Ea (eV)	Reference
$La_{0.6}Sr_{0.4}CoO_{3-\delta}$	350 nm	58.1	1.54	Garbayo et al. [42]
$(La_{0.6}Sr_{0.4})_{0.95}Co_{0.2}Fe_{0.8}O_3$	210 nm	24.8	1.50	Wells et al. [8]
$La_{0.6}Sr_{0.4}Co_{0.2}Fe_{0.8}O_{3-\delta}$ -$Ce_{0.8}Sm_{0.2}O_{1.9}$	30 μm	17.4	1.11	Ali et al. [30]
$(La_{0.71}Sr_{0.29})_{0.95}Co_{0.17}Fe_{0.83}O_{3-\delta}$	6 μm	0.92	1.5	Celikbilek et al. [22]
$La_{0.6}Sr_{0.4}Co_{0.2}Fe_{0.8}O_{3-\delta}$ - $Ce_{0.9}Gd_{0.1}O_{2-\delta}$ + $La_{0.6}Sr_{0.4}CoO_{3-\delta}$	300 nm + 1 μm	0.57	1.55	Develos-Bagarinao et al. [29]
$La_{0.6}Sr_{0.4}Co_{0.2}Fe_{0.8}O_{2.95}$ - YSZ	600 nm	0.55*	0.65	Lee et al. [14]
$La_{0.6}Sr_{0.4}CoO_{3-\delta}$ + $La_{0.6}Sr_{0.4}CoO_{3-\delta}$	200 nm + 40 μm	0.24	1.40	Hayd et al. [43]
$(La_{0.60}Sr_{0.40})_{0.95}Co_{0.20}Fe_{0.80}O_3$ - $(Sm_2O_3)_{0.20}(CeO_2)_{0.80}$	200 nm	0.03*	1.08	This work

highlighting the dependence of catalytic properties of perovskite oxides on the concentration of oxygen vacancies, which are typically induced through cation substitutions or A-site non-stoichiometry [45,47–49].

We therefore attribute the exceptionally low ASR of sample E to the formation of excess oxygen vacancies during the 700 °C vacuum annealing step of the deposition. [28] This is supported by Fig. 3(c), which shows the evolution of the ASR with up to 72 h spent at 430 °C in air. Here we observe that the initial performance remains stable for ~2 hrs, after which there is a rapid increase in ASR as a function of time, attributed to the filling of oxygen vacancies, which saturates after ~24 h. In this fully degraded state, the ASR of ~2×10^4 Ωcm^2 at 300 °C remains several orders of magnitude lower than the ~1×10^9 Ωcm^2 expected for dense LSCF thin films at this temperature, highlighting once again the advantages of the nanocomposite structure [28]. Critically, we

also demonstrate that by annealing the degraded sample in vacuum (700 °C for 40 min) the performance of the as grown sample can be fully restored. Nyquist plots for the sample at varying stages of degradation are shown in Fig. 3(d) and reveal that the impedance arc becomes slightly depressed with respect to the pristine sample upon degradation. This corresponds to the separation in the spectra of the features corresponding to each of the symmetric LSCF-SDC electrodes, most clearly visible in the sample degraded for 24 h. This separation is attributed to slightly differing degradation rates at each of the electrodes and is supported by the fact the impedance spectra can still be fit to the same equivalent circuit as the pristine sample (Table S2).

To further probe the oxygen content of the LSCF-SDC films in the present work, and understand the impact of the vacuum annealing process, additional samples were prepared on Si(001) substrates for ToF-ERDA and RBS measurements. Fig. 4 shows the ToF-vs-energy ERDA spectra of as-deposited and vacuum-annealed LSCF-SDC thin films together with their corresponding elemental depth-profiles. The ToF-vs-energy spectra in Fig. 4(a) and (b) contain signals from the films' constituents, Si substrate, and scattered iodine from the incident beam. The ToF-ERDA elemental depth-profiles of the as-deposited and vacuum-annealed LSCF-SDC films are exhibited in Fig. 4(c) and (d), respectively. Both depth-profiles show the existence of native oxide layers on the top surface of the thin films. Excluding the top-surface oxide layers, the plateaus in the depth-profiles prove uniform elemental distributions along the thickness of both films. The average ToF-ERDA elemental compositions, obtained from the plateau regions and given in the insets of Fig. 4(c) and (d), demonstrate a decrease in the O content from ~63.4 at % in the as-deposited film to ~60.1 at % in the annealed film.

The RBS experimental spectra and their corresponding SIMNRA simulations for the as-deposited and annealed samples are shown in Fig. 4(e) and (f), respectively. For both as-deposited and vacuum-annealed layers, only one single homogeneous model was employed to simulate the experimental data, indicating uniform elemental distributions that are in agreement with the ToF-ERDA results. Consistent with the ToF-ERDA driven compositions, the simulated RBS spectra also prove the O concentration decreases from ~63.3 at % to ~59.8 at % by vacuum annealing.

The next steps for future work are to induce stable oxygen vacancies into the LSCF. One of the most promising routes to achieve this is through doping of the LSCF lattice. Several studies demonstrate the introduction of dopants such as Sc, Nb, Co, Cu, Ag, Zn, Ni, Mg and Ce to the B-site cation to introduce oxygen vacancies into the lattice of various perovskite SOFC cathodes, in particular LSCF [34,44,45,47,48,49]. Characteristically, oxygen vacancies induced in this way have been shown not only to enhance the oxygen reduction kinetics of LSCF, but also to improve long-term stability. Therefore, by combining this approach with the unique deposition procedure for VAN oxygen electrodes outlined in the present work, one may anticipate the realisation of exceptionally low ASR oxygen electrodes with enhanced long-term stability.

3.6. *Characterising the complete rSOC structure (sample F)*

In characterising the complete rSOC structure we first studied whether processing of the cell at 700 °C disrupts the underlying Pt microstructure. This is particularly pertinent as several previous studies involving Pt report severe degradation at high temperatures (> 600 °C), due to agglomeration of the Pt limiting the availability of triple phase boundaries [14,16]. Fig. S6 shows top-down SEM images of the Pt following deposition at 600 °C (Fig. S6(a)) and 700 °C (Fig. S6(b)) which show little or no change in the Pt microstructure. Furthermore, Fig. S6(c) shows the microstructure remains unchanged after 72 h at 430 °C in air, indicating the long-term stability of the structure. Meanwhile, Fig. 6(d) shows the agglomeration of Pt once exposed to 700 °C in air, highlighting the importance of the vacuum conditions used during the final deposition/annealing step for preventing Pt agglomeration.

Measurements of the complete rSOC structure (sample F) were attempted under gas flows of synthetic air and dry hydrogen at the

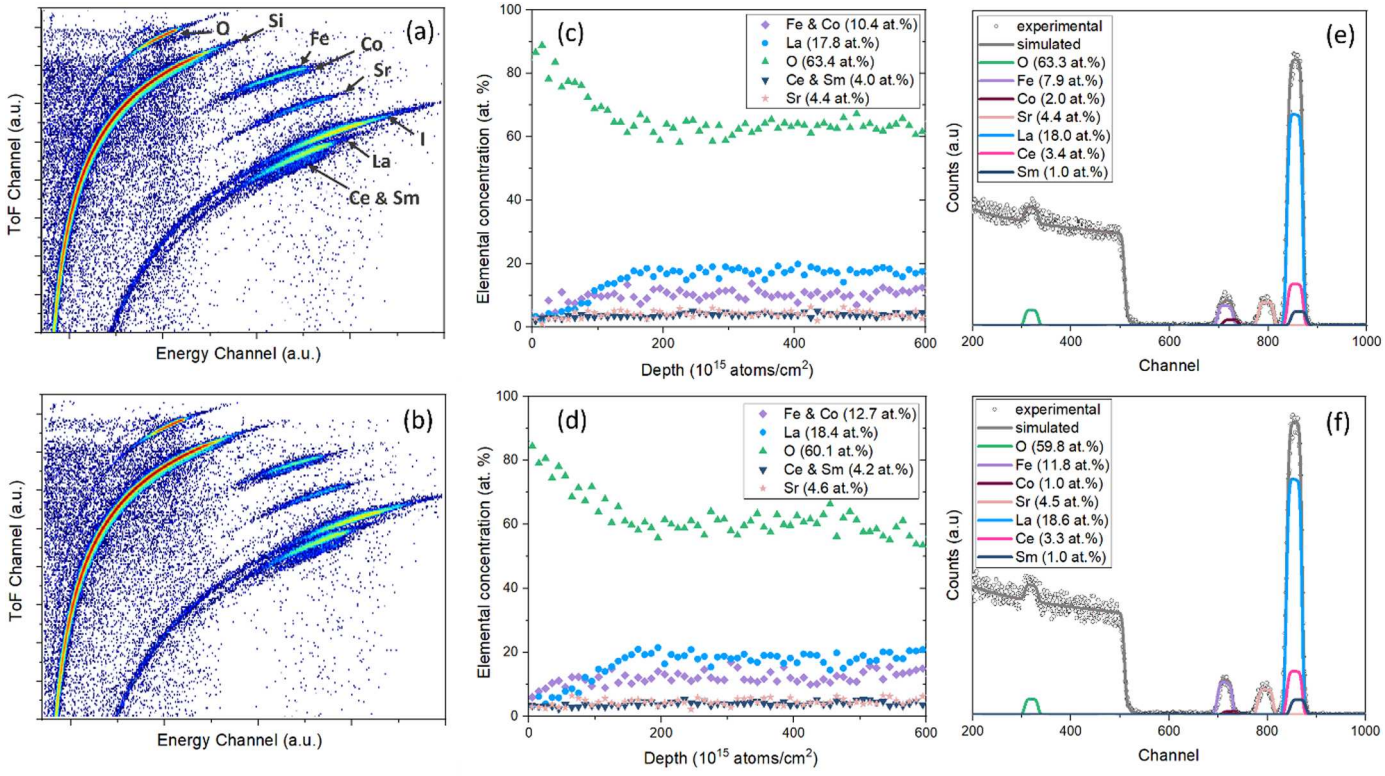

Fig. 4. ToF-vs-energy spectra for as-deposited (a) and annealed (b) LSCF-SDC films; ToF-ERDA elemental depth-profiles for as-deposited (c) and annealed (d) LSCF-SDC films; RBS experimental and fitted data for as-deposited (e) and annealed (f) LSCF-SDC films.

oxygen and fuel electrodes respectively. In the proof-of-concept device it was not possible to sustain a sufficient electrode contact and gas tight seal without damage to the device structure. This is attributed to the inherently fragile nature of the ~500 nm thick device deposited on ~60 μm thick porous alumina and reiterates the need for further engineering studies of fully thin-film based SOC devices. In particular, attention should be given to ensuring mechanical stability of the porous substrate, either through selection of alternative materials or optimisation of the substrate thickness. Further studies should also ensure the thin film electrolyte is of sufficient thickness to minimize the risk of gas leakage or of electrical short circuits through the application of excessive mechanical force during operation and testing. Nevertheless, the present work serves as a successful demonstration for a new route to achieving low ASR via oxygen vacancy tuning in nanocomposite thin films.

4. Conclusions

In this work we demonstrate to the best of our knowledge the lowest recorded ASR to date for a rSOC oxygen electrode. Indeed, below 500 °C the ASR of our LSCF-SDC is reduced by several orders of magnitude compared to previous state-of-the-art porous LSCF thin films. To achieve this, we first show that LSCF-SDC VAN films can be grown with high crystalline quality on single crystal YSZ substrates. Through electrochemical impedance spectroscopy we then reveal the LSCF-SDC system to have an exceptionally low activation energy of ~1.1 eV, allowing for state-of-the-art performance at low temperatures. Moreover, comparable ASR values are maintained when depositing instead on low-cost, commercially fabricated, porous alumina substrates. We then demonstrate growth of a complete rSOC structure, with the deposition process engineered such that the LSCF-SDC layer is in-situ annealed during deposition of the YSZ-Ni fuel electrode. This annealing process is shown to lead to a further reduction in the ASR of the LSCF-SDC by approximately 3 orders of magnitude. Consequently, we report here the first demonstration of a thin film rSOC oxygen electrode with ASR value $< 0.1\ \Omega cm^2$ at temperatures below 450 °C. We also outline a strategy for further stabilising this exceptional performance through the means of B-site doping of the LSCF lattice. In the present proof-of-concept device, the inability to sustain sufficient electrode contact and gas tight sealing highlights the need for further engineering studies to ensure mechanical stability of the thin-film device structures based on porous alumina. Overall, this work marks a major step towards the widespread implementation of future rSOC devices for portable power applications.

Funding sources

JLM-D and MPW acknowledge the European Union's Horizon 2020 research and innovation program [grant number 101017709] (EPISTORE). JLM-D also acknowledges support from the Royal Academy of Engineering Chair in Emerging technologies [grant number CIET1819_24], and the EPSRC Centre of Advanced Materials for Integrated Energy Systems (CAM-IES) [grant number EP/P007767/1] and the EU-H2020-ERC-ADG EROS [grant number 882929]. AJL acknowledges support from the EPSRC [grant number EP/R513180/1] and the Sir Henry Royce Institute [grant number EP/R00661X/1]. The (S)TEM work at Purdue University was supported by the U.S. National Science Foundation [grant numbers DMR-1809520 and DMR-2016453]. BB gratefully acknowledges financial support from Swedish Research Council (VR), grant no. 2019-00191 (for accelerator-based ion-technological centre in tandem accelerator laboratory in Uppsala University, Sweden) and grant no. 2021-00357, the University of Cambridge's "Knowledge Exchange and Impact award", Energy IRC Grants scheme, and CAPE BlueSky Research Award 2022.

CRediT authorship contribution statement

Matthew P. Wells, Judith L. MacManus-Driscoll: Conceptualization, Matthew P. Wells, Judith L. MacManus-Driscoll: Methodology, Matthew P. Wells, Adam J. Lovett: Validation, Matthew P. Wells, Adam J. Lovett, Yizhi Zhang, Zhongxia Shang, Babak Bakhit: Formal analysis, Matthew P. Wells, Adam J. Lovett, Yizhi Zhang, Zhongxia Shang, Kosova Kreka, Babak Bakhit: Investigation, Haiyan Wang, Albert Tarancón, Judith L. MacManus-Driscoll: Resources, Matthew P. Wells: Data curation, Matthew P. Wells: Writing – original draft, Matthew P. Wells, Adam J. Lovett, Yizhi Zhang, Zhongxia Shang, Kosova Kreka, Babak Bakhit, Haiyan Wang, Albert Tarancón, Judith L. MacManus-Driscoll: Writing – review and editing, Matthew P. Wells, Babak Bakhit: Visualization, Haiyan Wang, Albert Tarancón, Judith L. MacManus-Driscoll: Supervision, Matthew P. Wells: Project administration, Haiyan Wang, Babak Bakhit, Albert Tarancón, Judith L. MacManus-Driscoll: Funding acquisition.

Declaration of Competing Interest

The authors declare that they have no known competing financial interests or personal relationships that could have appeared to influence the work reported in this paper.

Data Availability

Data will be made available on request.

Appendix A. Supporting information

Supplementary data associated with this article can be found in the online version at doi:10.1016/j.nanoen.2023.109049.

References

[1] P. di Giorgio, U. Desideri, Potential of reversible solid oxide cells as electricity storage system, Energies (Basel) 9 (2016), https://doi.org/10.3390/en9080662.
[2] Y. Wang, A. Banerjee, L. Wehrle, Y. Shi, N. Brandon, O. Deutschmann, Performance analysis of a reversible solid oxide cell system based on multi-scale hierarchical solid oxide cell modelling, Energy Convers. Manag. 196 (2019), https://doi.org/10.1016/j.enconman.2019.05.099.
[3] F. Baiutti, F. Chiabrera, M. Acosta, D. Diercks, D. Parfitt, J. Santiso, X. Wang, A. Cavallaro, A. Morata, H. Wang, A. Chroneos, J. MacManus-Driscoll, A. Tarancon, A high-entropy manganite in an ordered nanocomposite for long-term application in solid oxide cells, Nat. Commun. 12 (2021), https://doi.org/10.1038/s41467-021-22916-4.
[4] M. Acosta, F. Baiutti, X. Wang, A. Cavallaro, J. Wu, W. Li, S.C. Paker, A. Aguadero, H. Wang, A. Tarancón, J.L. MacManus-Driscoll, Ultrafast oxygen reduction kinetics in (La,Sr)(Co,Fe)O3 vertically aligned nanocomposites below 400 °C, Submitted (2020).
[5] J. Yoon, S. Cho, J.H. Kim, J. Lee, Z. Bi, A. Serquis, X. Zhang, A. Manthiram, H. Wang, Vertically aligned nanocomposite thin films as a cathode/electrolyte interface layer for thin-film solid oxide fuel cells, Adv. Funct. Mater. 19 (2009) 3868–3873, https://doi.org/10.1002/adfm.200901338.
[6] J. Huang, J.L. MacManus-Driscoll, H. Wang, New epitaxy paradigm in epitaxial self-assembled oxide vertically aligned nanocomposite thin films, J. Mater. Res. 32 (2017) 4054–4066, https://doi.org/10.1557/jmr.2017.281.
[7] M. Acosta, F. Baiutti, A. Tarancón, J.L. MacManus-Driscoll, Nanostructured materials and interfaces for advanced ionic electronic conducting oxides, Adv. Mater. Interfaces 6 (2019), https://doi.org/10.1002/admi.201900462.
[8] M.P. Wells, A.J. Lovett, T. Chalklen, F. Baiutti, A. Tarancón, X. Wang, J. Ding, H. Wang, S. Kar-Narayan, M. Acosta, J.L. Macmanus-Driscoll, Route to high-performance micro-solid oxide fuel cells on metallic substrates, ACS Appl. Mater. Interfaces (2021), https://doi.org/10.1021/acsami.0c15368.
[9] S. Lee, J.L. MacManus-Driscoll, Research update: fast and tunable nanoionics in vertically aligned nanostructured films, APL Mater. 5 (2017), 042304, https://doi.org/10.1063/1.4978550.
[10] J.L. Macmanus-Driscoll, Self-assembled heteroepitaxial oxide nanocomposite thin film structures: Designing interface-induced functionality in electronic materials, Adv. Funct. Mater. 20 (2010) 2035–2045, https://doi.org/10.1002/adfm.201000373.
[11] X. Sun, J.L. MacManus-Driscoll, H. Wang, Spontaneous ordering of oxide-oxide epitaxial vertically aligned nanocomposite thin films, : Annu Rev. Mater. Res (2020) 229–253, https://doi.org/10.1146/annurev-matsci-091719-112806.

[12] A. Chen, Z. Bi, Q. Jia, J.L. Macmanus-Driscoll, H. Wang, Microstructure, vertical strain control and tunable functionalities in self-assembled, vertically aligned nanocomposite thin films, Acta Mater. 61 (2013) 2783–2792, https://doi.org/10.1016/j.actamat.2012.09.072.

[13] B. Zhu, G. Schusteritsch, P. Lu, J.L. Macmanus-Driscoll, C.J. Pickard, Determining interface structures in vertically aligned nanocomposite films, APL Mater. 7 (2019), https://doi.org/10.1063/1.5099204.

[14] Y.H. Lee, H. Ren, E.A. Wu, E.E. Fullerton, Y.S. Meng, N.Q. Minh, All-sputtered, superior power density thin-film solid oxide fuel cells with a novel nanofibrous ceramic cathode, Nano Lett. 20 (2020), https://doi.org/10.1021/acs.nanolett.9b02344.

[15] C. Fu, K. Sun, N. Zhang, X. Chen, D. Zhou, Electrochemical characteristics of LSCF-SDC composite cathode for intermediate temperature SOFC, Electro Acta 52 (2007), https://doi.org/10.1016/j.electacta.2007.01.001.

[16] A. Karimaghaloo, A.M. Andrade, S. Grewal, J.H. Shim, M.H. Lee, Mechanism of cathodic performance enhancement by a few-nanometer-thick oxide overcoat on porous Pt cathodes of solid oxide fuel cells, ACS Omega 2 (2017), https://doi.org/10.1021/acsomega.6b00433.

[17] M. Yu, X. Tong, B.R. Sudireddy, M. Chen, Performance and durability of reversible solid oxide cells with nano-electrocatalysts infiltrated electrodes, JOM 74 (2022), https://doi.org/10.1007/s11837-022-05540-5.

[18] Y. Wang, C. Wu, B. Zu, M. Han, Q. Du, M. Ni, K. Jiao, Ni migration of Ni-YSZ electrode in solid oxide electrolysis cell: an integrated model study, J. Power Sources 516 (2021), https://doi.org/10.1016/j.jpowsour.2021.230660.

[19] J.C. Ruiz-Morales, D. Marrero-López, J. Canales-Vázquez, J.T.S. Irvine, Symmetric and reversible solid oxide fuel cells, RSC Adv. 1 (2011), https://doi.org/10.1039/c1ra00284h.

[20] J. Grimes, J. Hong, S.A. Barnett, Effect of Gd-doped ceria infiltration into Ni-YSZ on reversible solid oxide cell operation, J. Power Sources 551 (2022), https://doi.org/10.1016/j.jpowsour.2022.232189.

[21] B. Bakhit, D. Primetzhofer, E. Pitthan, M.A. Sortica, E. Ntemou, J. Rosen, L. Hultman, I. Petrov, G. Greczynski, Systematic compositional analysis of sputter-deposited boron-containing thin films, J. Vac. Sci. Technol. A: Vac. Surf. Films 39 (2021), https://doi.org/10.1116/6.0001234.

[22] D. Özden Çelikbilek, E. Jauffrès, L. Siebert, M. Dessemond, C.L. Burriel, E. Djurado Martin, Rational design of hierarchically nanostructured electrodes for solid oxide fuel cells, J. Power Sources 333 (2016), https://doi.org/10.1016/j.jpowsour.2016.09.156.

[23] M. Machado, F. Baiutti, L. Bernadet, A. Morata, M. Nuñez, J.P. Ouweltjes, F. C. Fonseca, M. Torrell, A. Tarancón, Functional thin films as cathode/electrolyte interlayers: a strategy to enhance the performance and durability of solid oxide fuel cells, J. Mater. Chem. A Mater. 10 (2022), https://doi.org/10.1039/d2ta03641j.

[24] M. Shaban, M. Ali, K. Abdelhady, A.A.P. Khan, H. Hamdy, Hexagonal arrays of Pt nanocylinders on the top surface of PAA membranes using low vacuum sputter coating technique, Vacuum 161 (2019), https://doi.org/10.1016/j.vacuum.2018.12.039.

[25] B. Geboes, J. Ustarroz, K. Sentosun, H. Vanrompay, A. Hubin, S. Bals, T. Breugelmans, Electrochemical behavior of electrodeposited nanoporous Pt catalysts for the oxygen reduction reaction, ACS Catal. 6 (2016), https://doi.org/10.1021/acscatal.6b00668.

[26] M.T.Y. Paul, B.D. Gates, Mesoporous platinum prepared by electrodeposition for ultralow loading proton exchange membrane fuel cells, Sci. Rep. 9 (2019), https://doi.org/10.1038/s41598-019-38855-6.

[27] W. Luc, F. Jiao, Synthesis of nanoporous metals, oxides, carbides, and sulfides: beyond nanocasting, Acc. Chem. Res. 49 (2016), https://doi.org/10.1021/acs.accounts.6b00109.

[28] P. Plonczak, M. Søgaard, A. Bieberle-Hütter, P.V. Hendriksen, L.J. Gauckler, Electrochemical characterization of La 0.58 Sr 0.4 Co 0.2 Fe 0.8 O 3−δ thin film electrodes prepared by pulsed laser deposition, J. Electrochem Soc. 159 (2012) B471–B482, https://doi.org/10.1149/2.043204jes.

[29] K. Develos-Bagarinao, J. De Vero, H. Kishimoto, T. Ishiyama, K. Yamaji, T. Horita, H. Yokokawa, Oxygen surface exchange properties and surface segregation behavior of nanostructured La0.6Sr0.4Co0.2Fe0.8O3-δ thin film cathodes, Phys. Chem. Chem. Phys. 21 (2019) 7183–7195, https://doi.org/10.1039/c9cp00606k.

[30] S.A. Muhammed Ali, M. Anwar, L.S. Mahmud, N.S. Kalib, A. Muchtar, M. R. Somalu, Influence of current collecting and functional layer thickness on the performance stability of La 0.6 Sr 0.4 Co 0.2 Fe 0.8 O 3-δ -Ce 0.8 Sm 0.2 O 1.9 composite cathode, J. Solid State Electrochem. 23 (2019), https://doi.org/10.1007/s10008-019-04208-6.

[31] F. Shen, K. Lu, Comparison of different perovskite cathodes in solid oxide fuel cells, Fuel Cells 18 (2018), https://doi.org/10.1002/fuce.201800044.

[32] B.A. Boukamp, N. Hildenbrand, H.J.M. Bouwmeester, D.H.A. Blank, Impedance of thin film cathodes: thickness and current collector dependence, Solid State Ion. 283 (2015), https://doi.org/10.1016/j.ssi.2015.10.013.

[33] B. Koo, K. Kim, J.K. Kim, H. Kwon, J.W. Han, W.C. Jung, Sr segregation in perovskite oxides: why it happens and how it exists, Joule 2 (2018), https://doi.org/10.1016/j.joule.2018.07.016.

[34] M. Acosta, F. Baiutti, X. Wang, A. Cavallaro, J. Wu, W. Li, S.C. Parker, A. Aguadero, H. Wang, A. Tarancón, J.L. MacManus-Driscoll, Surface chemistry and porosity engineering through etching reveal ultrafast oxygen reduction kinetics below 400 °C in B-site exposed (La,Sr)(Co,Fe)O3 thin-films, J. Power Sources 523 (2022), https://doi.org/10.1016/j.jpowsour.2022.230983.

[35] A.K. Opitz, A. Lutz, M. Kubicek, F. Kubel, H. Hutter, J. Fleig, Investigation of the oxygen exchange mechanism on Ptyttria stabilized zirconia at intermediate temperatures: surface path versus bulk path, Electro Acta 56 (2011), https://doi.org/10.1016/j.electacta.2011.07.112.

[36] A. Karimaghaloo, A.M. Andrade, S. Grewal, J.H. Shim, M.H. Lee, Mechanism of cathodic performance enhancement by a few-nanometer-thick oxide overcoat on porous Pt cathodes of solid oxide fuel cells, ACS Omega 2 (2017), https://doi.org/10.1021/acsomega.6b00433.

[37] R. Gao, A. Fernandez, T. Chakraborty, A. Luo, D. Pesquera, S. Das, G. Velarde, V. Thoréton, J. Kilner, T. Ishihara, S. Nemšák, E.J. Crumlin, E. Ertekin, L. W. Martin, Correlating surface crystal orientation and gas kinetics in perovskite oxide electrodes, Adv. Mater. 33 (2021), https://doi.org/10.1002/adma.202100977.

[38] J. Jiang, X. Hu, N. Ye, J.L. Hertz, Microstructure and ionic conductivity of yttria-stabilized zirconia thin films deposited on MgO, J. Am. Ceram. Soc. 97 (2014), https://doi.org/10.1111/jace.12740.

[39] J.T.S. Irvine, D.C. Sinclair, A.R. West, Electroceramics: characterization by impedance spectroscopy, Adv. Mater. 2 (1990), https://doi.org/10.1002/adma.19900020304.

[40] Q. Su, D. Yoon, A. Chen, F. Khatkhatay, A. Manthiram, H. Wang, Vertically aligned nanocomposite electrolytes with superior out-of-plane ionic conductivity for solid oxide fuel cells, J. Power Sources 242 (2013), https://doi.org/10.1016/j.jpowsour.2013.05.137.

[41] J. Jiang, J.L. Hertz, On the variability of reported ionic conductivity in nanoscale YSZ thin films, J. Electroceram 32 (2014) 37–46, https://doi.org/10.1007/s10832-013-9857-1.

[42] Muhammed Ali S.A, J. Raharjo, M. Anwar, D.S. Khaerudini, A. Muchtar, L. Spiridigliozzi, M.R. Somalu, Carbonate-based lanthanum strontium cobalt ferrite (LSCF)-samarium-doped ceria (SDC) composite cathode for low-temperature solid oxide fuel cells, Appl. Sci. (Switz.) 10 (2020), https://doi.org/10.3390/app10113761.

[43] J. Hayd, H. Yokokawa, E. Ivers-Tiffée, Hetero-interfaces at nanoscaled (La,Sr)CoO 3-δ thin-film cathodes enhancing oxygen surface-exchange properties, J. Electrochem Soc. 160 (2013), https://doi.org/10.1149/2.017304jes.

[44] D. Mantzavinos, A. Hartley, I.S. Metcalfe, M. Sahibzada, Oxygen stoichiometries in La1-xSrxCo1-yFeyO3-δ perovskites at reduced oxygen partial pressures, Solid State Ion.-. 134 (2000), https://doi.org/10.1016/S0167-2738(00)00718-9.

[45] Q. Ji, L. Bi, J. Zhang, H. Cao, X.S. Zhao, The role of oxygen vacancies of ABO3perovskite oxides in the oxygen reduction reaction, Energy Environ. Sci. 13 (2020), https://doi.org/10.1039/d0ee00092b.

[46] Y. Cao, M.J. Gadre, A.T. Ngo, S.B. Adler, D.D. Morgan, Factors controlling surface oxygen exchange in oxides, Nat. Commun. 10 (2019), https://doi.org/10.1038/s41467-019-08674-4.

[47] W. Zhou, R. Ran, Z. Shao, W. Jin, N. Xu, Evaluation of A-site cation-deficient (Ba0.5Sr0.5)1-xCo0.8Fe0.2O3-δ (x > 0) perovskite as a solid-oxide fuel cell cathode, J. Power Sources 182 (2008), https://doi.org/10.1016/j.jpowsour.2008.04.012.

[48] J. Faye, A. Baylet, M. Trentesaux, S. Royer, F. Dumeignil, D. Duprez, S. Valange, J. M. Tatibouët, Influence of lanthanum stoichiometry in La 1-xFeO 3-δ perovskites on their structure and catalytic performance in CH 4 total oxidation, Appl. Catal. B 126 (2012), https://doi.org/10.1016/j.apcatb.2012.07.001.

[49] J. Xu, C. Chen, Z. Han, Y. Yang, J. Li, Q. Deng, Recent advances in oxygen electrocatalysts based on perovskite oxides, Nanomaterials 9 (2019), https://doi.org/10.3390/nano9081161.